ACS APPLIED ENERGY MATERIALS

www.acsaem.org Article

Selective Water Oxidation to H_2O_2 on TiO_2 Surfaces with Redox-Active Allosteric Sites

Dongyu Liu, Devan Solanki, Eli Stavitski, Mingtao Li, Shu Hu,* Victor S. Batista,* and Ke R. Yang*

Cite This: *ACS Appl. Energy Mater.* 2023, 6, 8368−8376 Read Online

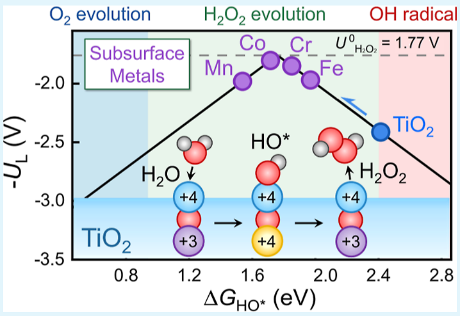

ABSTRACT: Generation of hydrogen peroxide (H_2O_2) by electrocatalytic water oxidation is a promising approach for renewable energy utilization that motivates the development of selective catalytic materials. Here, we report a combined theoretical and experimental study, showing that alloyed TiO_2 electrodes embedded with subsurface redox-active transition metals enable water oxidation to H_2O_2 at low overpotentials. Density functional theory calculations show that first-row transition metals (Cr, Mn, Fe, and Co) serve as reservoirs of oxidizing equivalents that couple to substrate binding sites on the surface of redox-inert metal oxides. The distinct sites for substrate binding and redox state transitions reduce the overpotential of the critical first step of water oxidation, the oxidization of H_2O* to HO* ("*" = adsorbed), enhancing the selectivity for H_2O_2. Electrochemical analysis of alloyed TiO_2 electrodes with subsurface Mn fabricated by atomic layer deposition confirms the theoretical predictions, showing enhanced selectivity for H_2O_2 generation (>90%) due to a significant shift of the onset potential (1.8 V vs reversible hydrogen electrode (RHE)), a 500 mV cathodic shift when compared to pristine TiO_2 (2.3 V vs RHE). These findings show that otherwise inert metal oxides with subsurface redox-active sites represent a promising class of catalytic materials for a wide range of applications due to the uncoupling of substrate binding and catalytic redox-state transitions.

KEYWORDS: *selective water oxidation, electrocatalysis, hydrogen peroxide production, titanium dioxide, redox-active transition metal, density functional theory, subsurface single atom catalyst*

1. INTRODUCTION

Electrochemical generation of hydrogen peroxide (H_2O_2) by water oxidation is a promising approach for renewable energy utilization.[1−4] However, the large-scale application of this attractive two-electron oxidation reaction remains limited by the lack of efficient catalysts based on inexpensive materials.[5,6] Recent studies have revealed that the first step of the reaction likely converts surface-bound water to hydroxyl species, an elementary process thought to play a dominant role in controlling the overall catalytic performance.[7−9] Here, we introduce catalytic materials based on inexpensive metal oxides that facilitate the critical first step of the water oxidation reaction (WOR) and enable efficient generation of H_2O_2 at low overpotentials with significant selectivity over oxygen evolution.

H_2O_2 is a versatile and environmentally benign oxidant as it has a high oxidation potential over the whole range of pH[10] and produces only water as a byproduct. H_2O_2 is used in a wide range of industrial processes from paper bleaching to chemical synthesis and has great potential as a high-density energy carrier.[10,11] Synthesis of H_2O_2 is currently based mostly on the energy-intensive anthraquinone process, which requires large-scale industrial facilities and significant safety precautions regarding storage and transportation.[12,13] Therefore, there is a significant interest in realizing electrochemical methods for distributed on-site H_2O_2 production, a process which could be powered by renewable solar and wind energy.[14−16] Currently, most studies of electrochemical generation of H_2O_2 are focused on O_2 reduction, while water oxidation is another attractive pathway to convert water and electric energy into high-value-added chemicals.[17−19]

The main outstanding challenge for H_2O_2 production via the 2e-WOR is the development of selective electrocatalysts capable of operating at low overpotentials.[20] Water oxidation to H_2O_2, with a potential of 1.77 V vs standard hydrogen electrode (SHE), is usually outcompeted by the thermodynamically less demanding oxygen evolution reaction (a 4e-WOR with a standard potential of 1.23 V vs SHE).[9] To date, only a few materials have been shown to preferentially produce H_2O_2, notably ZnO, $BiVO_4$, $CaSnO_3$, SnO_2, TiO_2, and WO_3.[8,21,22] We note that those materials are all redox-inert metal oxides (i.e., with metals that remain redox-inactive in their highest oxidation state). These metal oxides cannot be

Received: April 27, 2023
Accepted: August 3, 2023
Published: August 15, 2023

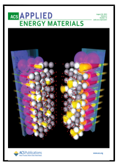

https://doi.org/10.1021/acsaem.3c01057

further oxidized, so the oxidation involves electron removal from adsorbed water, a process that usually requires high overpotentials (ΔG_{HO*} much larger than 1.77 eV vs SHE) and forms highly unstable surface-bound hydroxyl radical intermediates, HO* (* = surface adsorbed).[7] Therefore, reducing ΔG_{HO*} is critical to favor H_2O_2 generation at low overpotentials. Recently, introducing dopants or oxygen vacancies into such redox-inert metal oxides is demonstrated to effectively improve the performance of selective water oxidation toward H_2O_2, where we believe that these defects play a key role in modulating the redox properties of the host materials.[23−26] Thus, it is clear that the search for efficient electrocatalysts should benefit from an analysis of the correlation between the reactivity of the redox process, the energy level of the charge transfer processes, and 2e-WOR activity.

Theoretical studies have suggested that the activity trend of electrochemical water oxidation can be expressed as a function of ΔG_{HO*} which is defined as the free energy of oxidation of water to form HO* on the surface.[21,22,27] In particular, ΔG_{HO*} should be kept as close as possible to 1.77 eV vs SHE to enhance the generation of H_2O_2.[7−9] Here, we introduce a new strategy to synthesize materials which achieve those properties by embedding redox-inert metal-oxide surfaces with subsurface redox-active transition metals. We combine theoretical modeling based on density functional theory (DFT) and utilize atomic layer deposition (ALD) to demonstrate that growing TiO_2 with embedded redox-active transition metals below the surface is an effective approach to synthesize catalytic surfaces that tune ΔG_{HO*} toward H_2O_2 production. This synthesis method enables decoupling the adsorption/desorption binding energy determined by the surface from the redox activity of the sub-surface atoms, enabling deviation from the otherwise linear scaling relationship of the two. Embedding redox-active metals beneath the surface enables catalysis by first-row transition metals over a wide range of pH, preventing conditions that favor low oxidation states or protonation of oxo-bridges conditions which make redox-active metal oxides otherwise unstable in aqueous solutions.

The working mechanism is schematically illustrated in Scheme 1. We focus on Cr, Mn, Fe, and Co as redox-active centers embedded in TiO_2 and explore their functionality through analysis of redox potentials, electronic structures, and density of states (DOSs). Thermodynamic calculations and spin density analysis allow us to investigate the impact of embedded metals on substrate binding energies and reaction energy profiles. Moreover, analysis of the activity volcano curve and selectivity phase diagram with respect to the limiting potentials for the generation of O_2 and H_2O_2 elucidate the structure/function relationship of these materials and provide avenues for performance improvement.

2. METHODS

DFT calculations were performed with periodic boundary conditions using the Vienna Ab Initio Simulation Package (VASP) version 5.4.[28−31] Spin-polarized Kohn−Sham calculations were performed to describe the open-shell species. The projector augmented wave method[32,33] and the Perdew−Burke−Ernzerhof exchange−correlation functional[34] were employed to describe electron−ion interactions. A plane-wave cutoff energy of 500 eV was adopted for all computations, and the Brillouin zone was integrated using a Gaussian smearing method with $\sigma = 0.05$ eV. Electronic and ionic optimizations were carried out with an energy change criterion of 10^{-5} eV per supercell and a maximum force criterion of 0.02 eV/Å, respectively. The empirical DFT + *U* method, following Dudarev's approach,[35] was applied to describe strongly correlated d electrons in transition metals. Effective Hubbard-type $U_{eff} = U - J$ parameters of 3.5, 3.9, 4.0, and 3.5 eV were used for Cr, Mn, Fe, and Co, respectively.[36−39] Moreover, the London dispersion interaction was considered with Grimme's DFT-D3 method, with Becke−Johnson damping.[40,41]

Scheme 1. (a) HO* Formation on TiO_2 Surfaces without Subsurface Redox-Active Transition Metals; (b) HO* Formation on TiO_2 Surfaces with Subsurface Redox-Active Transition Metals

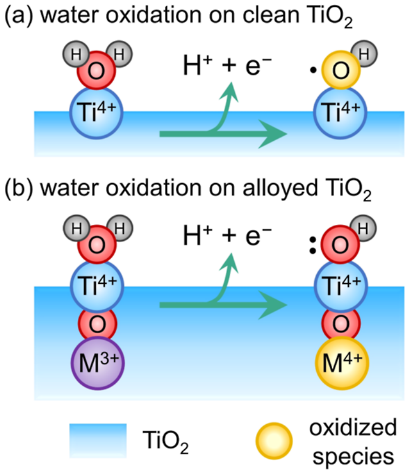

Bulk rutile TiO_2 was fully relaxed using a 7 × 7 × 11 Monkhorst−Pack type *k*-points mesh,[42] and the optimized lattice parameters $a = b = 4.606$ Å and $c = 2.961$ Å are in good agreement with experimental results.[43] The TiO_2 surface was represented by the thermodynamically most stable (110) facet,[44] which was modeled using a 2 × 1 supercell (along the [001] and [$1\bar{1}0$] directions) consisting of five O−Ti−O trilayers with a 3 × 3 × 1 Monkhorst−Pack *k*-point mesh. A vacuum layer of 16 Å along the *z*-axis was introduced to avoid the artificial interactions between periodically repeating images. To consider the interaction between water and surface, both terminals of the TiO_2 slabs were saturated by water molecules.[45,46] Especially, the water molecules at bottom were dissociated to reduce the lattice distortion.[47] The water adsorption configuration was obtained by relaxing the pristine TiO_2 slab with the fourth layer frozen. And in subsequent calculations, the bottom two layers as well as the water at the bottom were fixed to mimic bulk properties. The DOS was calculated with the HSE06 hybrid functional[48] using a 5 × 5 × 1 Monkhorst−Pack *k*-point mesh, and the energy range was converted to the potential of SHE by considering a value of 4.44 eV relative to the vacuum level.[49]

The reaction mechanisms of water oxidation toward the generation of O_2 and H_2O_2 were considered by analyzing HO*, O*, and HOO* as intermediates.[9] Thermodynamic corrections of the zero-point energy, enthalpy, and entropy at 298 K were included to calculate free energies using the VASPKIT code.[50] Especially, the free energies of O_2 and H_2O_2 were derived from their standard redox potentials.[21] The chemical potential of the proton and electron pair was treated with the computational hydrogen electrode (CHE) model, which defines $\mu(H^+ + e^-) = 1/2\ \mu(H_2)$ under the standard conditions.[51] Therefore, the calculated potentials are referred to SHE by definition. The theoretical activity and selectivity of water oxidation on different models were evaluated with the limiting potential (U_L), which is defined as the lowest potential to make all the electrochemical reaction steps downhill in free energy.[7] A smaller U_L indicates a lower overpotential, in agreement with experimental onset potentials.[7,8]

Reaction pathway for O_2 evolution

$$H_2O^* \rightarrow HO^* + H^+ + e^- \tag{1a}$$

$$HO^* \rightarrow O^* + H^+ + e^- \tag{1b}$$

$$O^* + H_2O(l) \rightarrow HOO^* + H^+ + e^- \quad (1c)$$

$$HOO^* + H_2O(l) \rightarrow H_2O^* + O_2\uparrow + H^+ + e^- \quad (1d)$$

Reaction pathway for H_2O_2 evolution

$$H_2O^* \rightarrow O^* + H^+ + e^- \quad (2a)$$

$$HO^* + 2H_2O(l) \rightarrow H_2O^* + H_2O_2(aq) + H^+ + e^- \quad (2b)$$

We alloyed TiO_2 with redox-active Cr, Mn, Fe, and Co ions since those metal centers are all earth-abundant first-row transition metals, particularly effective at catalyzing water oxidation in homogeneous catalysts.[52−54] Embedded as subsurface centers in TiO_2, the ions are oxidized, promoting the first reaction step by decreasing the corresponding ΔG_{HO^*}, as required for the oxidation of water to HO*. These redox-active metals are embedded in the TiO_2 crystal by replacing subsurface Ti^{4+} ions with ions of similar charge and radius. The top TiO_2 protective layer prevents redox-active metals from leaching into the solution, thus enhancing their stability and functionality during catalysis as they cycle through different oxidation states.[55] Changes in the oxidation state typically involve changes in the protonation state of oxo bridges on the surface keeping charge neutrality of the alloyed TiO_2 lattice (e.g., replacement of Ti^{4+} by Mn(III) has an adjacent protonated oxo bridge), analogous to interstitial protons that are common impurities in TiO_2 when an additional electron forms Ti^{3+} with a rather high n-type carrier concentration.[56,57] The subsurface redox-active transition metals are experimentally realized by growing a TiO_2 layer on top of the redox-active transition metal ions by ALD.[55,58]

We have synthesized TiO_2 surfaces with subsurface Mn by growing a 5 nm TiO_2 layer by ALD, incorporating Mn(III) to form $TiMnO_x$ by treatment with tris(tetramethyl-heptanedionato) Mn(III), using ozone as the primary oxidant. Tetrakis-dimethylamido-Ti(IV) and water were used as previously reported.[59] One MnO_x ALD cycle is applied for every eight TiO_2 cycles (i.e., 8:1 $TiMnO_x$ which was measured to have 26.7% Mn and 73.3% Ti among all cations in the oxide[59]). The resulting microstructure is amorphous, with distributed Mn atomistic positions in amorphous $TiMnO_x$. This is verified experimentally by X-ray diffraction which shows the absence of any crystalline feature (Supporting Information Section S8). Four TiO_2 cycles were grown to cap the last MnO_x cycle. The growth rate was measured before starting the growth to ensure that there is a complete surface coverage of TiO_2 during deposition. These films were grown on both fluorine-doped tin oxide (FTO) and Cr-alloyed TiO_2 ($TiCrO_x$)-coated FTO.

The electrochemical behavior of $(Ti,Mn)O_x$ electrodes was measured in a three-electrode setup. A Bio-Logic S200 potentiostat system connected the $TiMnO_x$ working electrode, a saturated calomel reference electrode, and a Ti foil counter electrode in a 0.5 M phosphate buffer (PB) solution at pH 7.4 at room temperature with stirring. The electrolyte was purified using a two-electrode setup where 3.5 V was applied between two planar Ti electrodes. The solution was then purged with N_2 30 prior to electrolysis. Figures are plotted in IUPAC convention, and the potentials are IR-corrected. The scans were started at 0.5 V vs RHE and swept anodically first at 20 mV/s.

Product accumulation was carried out in an H-cell configuration with a Nafion 117 membrane separating the $TiMnO_x$ working electrode from the Ti foil counter electrode. H_2O_2 quantification was achieved by the recommended $KMnO_4$-based spectrophotometric method (Section S5). O_2 was not necessary due to the high FE toward H_2O_2 production.[60] Prior to electrolysis, all glassware was cleaned via an RCA-2 etching process to remove trace metal impurities, in particular iron and copper impurities, which has been shown to decompose H_2O_2. Care was taken not to use metal clamps for holding down the reactor vessel. Electrolysis was performed in the complete dark to prevent UV-initiated degradation.

3. RESULTS AND DISCUSSION

Figure 1 shows the model structures of TiO_2 (110) slabs with subsurface redox-active metals. Ti^{4+} ions have octahedral coordination to six O atoms, with four O atoms defining an equatorial plane and two other O atoms with longer Ti−O distances along the perpendicular axis. Thus, there are two sites to introduce a redox-active transition metal ion in the subsurface layer of TiO_2 (110). Site A corresponds to the longer Ti−O bond parallel to the (110) surface, while site B corresponds to the longer Ti−O bond perpendicular to the (110) surface. Since we introduce protons to maintain the lattice charge neutrality using M(III) (M = Cr, Mn, Fe, and Co), we test the relative stability of the models with H at different oxo bridges adjacent to the M(III) impurity. As expected, the lowest energy structures correspond to models with the protonated oxo bridge along the long axis, consistent with the Jahn−Teller distortion (see Figure S1), so they are used for our thermodynamic and reactivity analysis. More details are given in the Supporting Information (Section S1).

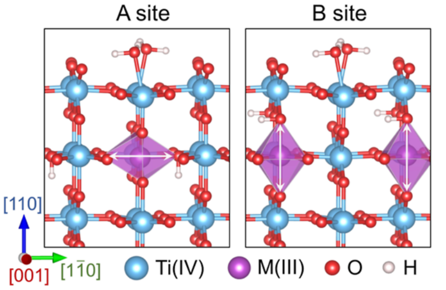

Figure 1. Structures of model TiO_2 slabs with subsurface redox-active transition metals (M = Cr, Mn, Fe, and Co). The longer axes in the octahedron are denoted with white arrows.

We calculated the DOS of the optimized structural models to analyze the energy level alignment as determined by the electronic structure (Figure 2). Only results for the A site are given here due to the similarities between the metal atoms alloyed at different sites (see Section S2). We find that the embedded transition metals negligibly shift the states of Ti and O atoms but introduce occupied states close to the valence band maximum. Electrons at these newly created states are preferentially removed by oxidation reactions due to their

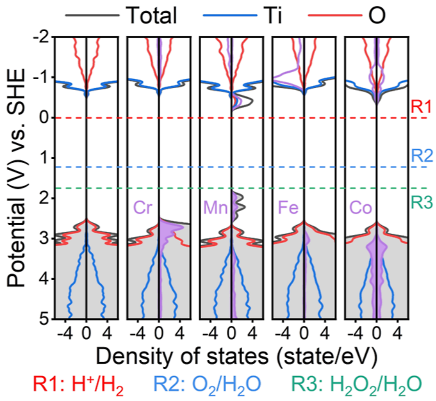

Figure 2. Element-projected DOS of pristine TiO_2 and models with subsurface redox-active metal ions at the A site. The filled regions indicate occupied states.

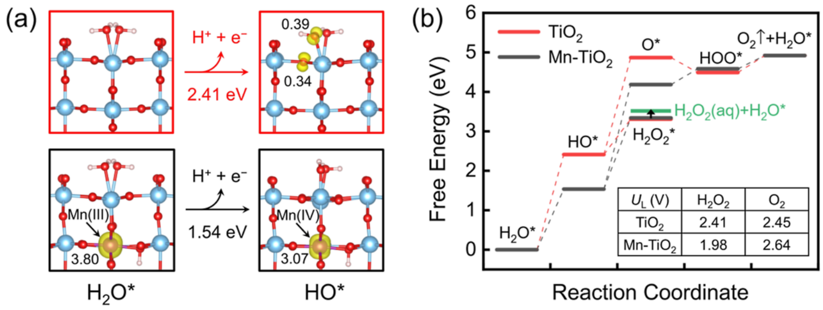

Figure 3. (a) DFT-optimized structural models of H_2O* and HO* on the pristine (red boxes) and Mn-alloyed (black boxes) TiO_2 (110) surfaces and free energy change of the first oxidation step. The yellow iso-surface (0.03 e/bohr^3) shows the spin density distribution. Atomic magnetic moments of the corresponding ions are shown in μ_B. The color code is the same as in Figure 1. (b) Free energy diagrams of water oxidation on the pristine and Mn-alloyed TiO_2 surfaces. The inset table shows the limiting potential (U_L) toward different products on the two surfaces, where U_L is defined as the lowest potential to make all the electrochemical reaction steps downhill in free energy.[7]

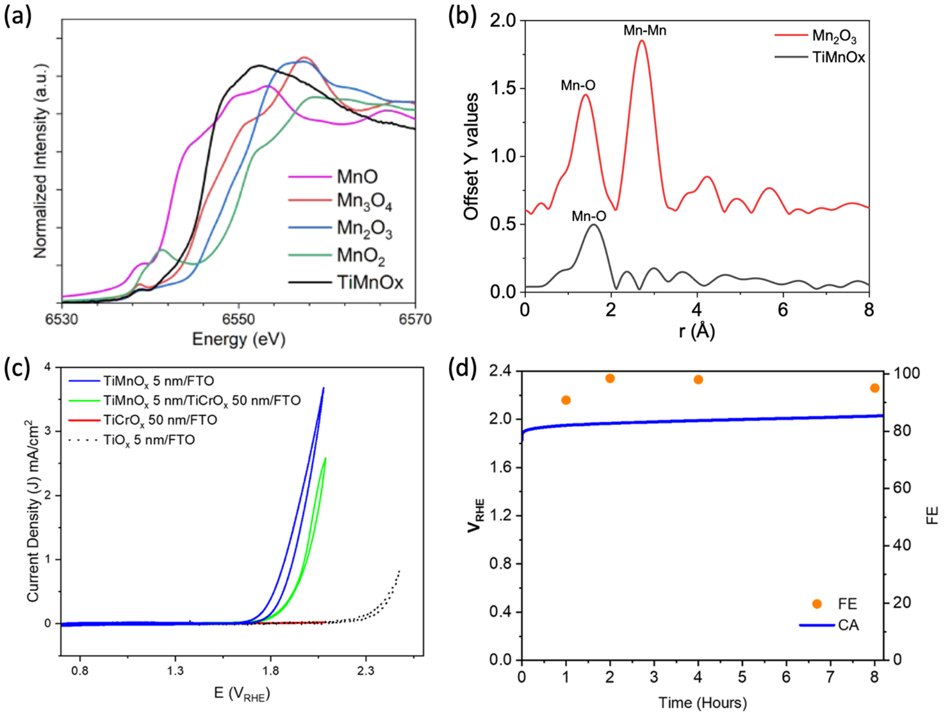

Figure 4. Performance and structural characterization of the $TiMnO_x$ electrocatalytic surface. (a) XANES of Mn K-edge $TiMnO_x$ alongside references. (b) Fourier-transformed EXAFS of $TiMnO_x$ alongside Mn_2O_3 reference. (c) Current density−potential (J−E) behavior of the $TiMnO_x$ electrocatalytic coating on FTO and $TiCrO_x$-coated FTO substrate, measured in 0.5 M pH = 7.4 PB at a scan rate of 20 mV·s^{-1}. (d) Chronoamperometry and corresponding FE measurements of $TiMnO_x$ performed at 1 mA/cm^2. Errors bars capture 3 repetitions and instrument precision.

relative high energies and therefore require lower overpotentials for water oxidation to HO* since they reduce the corresponding ΔG_{HO*}. In addition, Mn narrows the band gap by inducing occupied impurity states in the band gap while keeping the band edge properly aligned for water splitting toward H_2 and H_2O_2 generation. These features suggest that besides boosting the electrochemical process, Mn can further sensitize TiO_2 to enable visible light-driven photoelectrochemical H_2O_2 generation.

Next, we use the A site surface model of Mn-alloyed TiO_2 to investigate the influence of the redox-active metal center on water oxidation. Figure 3a shows the optimized structures and spin density distributions of H_2O* and HO* on pristine and Mn-alloyed TiO_2 surfaces, corresponding to the states before and after undergoing the crucial first step of the WOR. On the pristine TiO_2 (110) surface, HO* is expected to be oxidized since Ti^{4+} centers are already in their highest oxidation state. However, the spin density is found to be delocalized between HO* and a lattice oxo bridge, indicating strong coupling between these two O centers, consistent with studies of photooxidation of water on TiO_2 surfaces.[61,62] Considering that the hydroxyl radical HO* is a highly reactive species, it is expected to react with the strongly coupled lattice oxo bridge and form a surface-bound Ti−O−O−Ti peroxo intermediate, consistent with in situ FTIR measurements,[63] and eventually be further oxidized and released as a dioxygen molecule. Moreover, two adjacent HO* can react to generate H_2O_2.

Theoretically, TiO_2 should have good selectivity for 2e-WOR toward H_2O_2, although experimentally it exhibits low Faraday efficiency (FE),[8] likely due to the reactivity of the

HO* radical. In contrast, on Mn-alloyed TiO_2 surfaces, the spin density distribution indicates that the subsurface Mn(III) is oxidized to Mn(IV) after the formation of HO*, which confirms that the introduced redox-active metals serve as an electron reservoir to facilitate the first oxidation step. In addition, the absence of the reactive HO* radical suppresses potential side reactions, thereby enhancing the selectivity toward H_2O_2 production. From the thermodynamic point of view, the voltage required to generate H_2O_2 is greatly reduced from 2.41 V vs SHE on the pristine TiO_2 surface to 1.98 V vs SHE on the Mn-alloyed TiO_2 surface. Details on the analysis of spin density distributions and reaction free energy profiles for all the different models investigated are provided in the Supporting Information, Section S3.

The impact of redox-active metals on the electrochemical H_2O_2 generation can be further analyzed by using the free energy diagrams shown in Figure 3b. On the pristine TiO_2 (110) surface, the ΔG_{HO*} is significantly higher than the ideal value of 1.77 eV, leading to high overpotentials for H_2O_2 evolution. The highly reactive surface-bound hydroxyl radical HO* can lead to side reactions compromising the reaction selectivity. With Mn(III) as an electron reservoir, the ΔG_{HO*} is significantly reduced. Remarkably, the large ΔG of the subsequent oxidation from HO* to O* is barely affected by Mn(IV) since that high valent state of Mn would require a much even higher potential to be further oxidized to Mn(V) in the subsurface site. These results reveal that subsurface redox-active metals promote the oxidation of water to HO* while maintaining the unfavorable generation of O* as on pristine TiO_2 surfaces, thus selectively enhancing the H_2O_2 evolution reaction. The subsequent free energy changes for the steps that form H_2O_2* and HOO* are nearly maintained since those transformations do not involve redox state transitions of sites on the metal oxide surface. Remarkably, similar trends are observed for the free energy profiles of Cr, Mn, Fe, and Co in different sites (as detailed in Supporting Information, Section S4).

As shown in Figure 4a, the Mn average oxidation state is between 2+ and 3+ and resembles that of Mn_3O_4 as determined by the absorption K-edge and referenced against MnO, Mn_3O_4, Mn_2O_3, and MnO_2 powder standards. The extended-X-ray absorption fine structure (EXAFS) analysis of the Mn K-edge (Figure 4b) shows that the as-grown Mn-alloyed TiO_2 has only one peak, corresponding to a well-defined first coordination shell. The second peak observed in the Mn_2O_3 reference data that indicates Mn−O−Mn bonds (Figure 4b) is absent in the TiMnOx sample, indicating that the Mn ions are amorphous and atomically dispersed single-site redox-active centers, surrounded by Ti ions via oxo bridges. Thus, the microstructures of these films are representative of the atomistic structures in DFT modeling.

Figure 4c compares the current density−potential behavior of Mn-alloyed TiO_2, pure rutile TiO_2, and $TiCrO_x$ surfaces. $TiMnO_x$ on FTO is the electrode of interest; however, care was taken to understand the effect of the tin oxide substrate on performance. The $TiCrO_x$ film is conductive and metallic but catalytically inactive in this potential window. Thus, $TiCrO_x$ was chosen as a contact layer to verify that the catalytic behavior was not due to the fluorine-doped SnO_2 (FTO) underlayer as SnO_2 has been shown to be capable of producing hydrogen peroxide.[64] Pristine TiO_2 required a significant overpotential of over 500 mV to achieve 1 mA/cm^2. The onset potential at ca. 1.80 V vs RHE for Mn-alloyed TiO_2 indicates that the subsurface Mn atoms enable water oxidation activity, whereas the onset potential of ca. 2.3 V vs RHE for pure rutile TiO_2 can be partially attributed to the lack of redox-active centers.

Water oxidation by the $TiMnO_x$ electrodes in an electrochemical H-cell (see Methods for detailed procedures) was carried out over 8 h (Figure 4d) in the potential range of 1.80−2.00 V vs RHE. The electrodes were held at 1 mA/cm^2, and the potential was free to adjust to maintain that current density. The FE toward H_2O_2 production was measured between the time points and not taken to be cumulative. Thus, the data points represent the discrete time points between hours 0−1, 1−2, 2−4, and 4−8 to minimize carryover error to the next measurement. The FE was >90% for all time points, showing good selectivity toward H_2O_2 and that TiO_2 termination was successful in fabricating a surface that does not decompose H_2O_2. Constant current measurement limit changes in the production rate of hydrogen peroxide to catalytic selectivity as a function of electrode potential. In a further experiment, the system was operated at a constant current for 50 h to measure the stability of the catalyst and verify that the elemental composition of the alloy remained stable throughout operation (Section S6). Linear sweep voltammetry, LSV, was conducted with and without iR correction to determine the operating conditions to conduct electrolysis near 1.0 mA/cm^2 (Section S7). After 50 h of constant current electrolysis at 1.0 mA/cm^2, the overpotential required to drive the current rose from 100 mV at $t = 5$ h to 150 mV at $t = 50$ h. The significant lower onset potential of the amorphous Mn-alloyed TiO_2 and its drastically higher water-oxidation activity relative to pristine TiO_2 partially validate our computational analysis of the catalytic role of Mn subsurface ions.

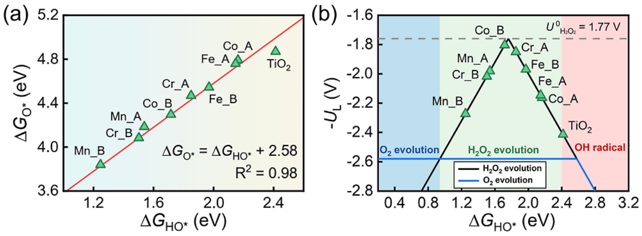

Figure 5. (a) Linear scaling relationship between ΔG_{HO*} and ΔG_{O*} on different surfaces. (b) Theoretical activity volcano and selectivity plot based on calculated limiting potentials (U_L) as a function of ΔG_{HO*} for O_2 evolution (blue line) and H_2O_2 evolution (black line).

Figure 5a shows the effect of different subsurface redox-active metal centers on the free energy changes ΔG_{HO*} and ΔG_{O*}. It demonstrates a linear relationship with direct correlation between the two free energy changes $\Delta G_{O*} = \Delta G_{HO*} + 2.58$ eV, indicating that the ΔG for the oxidation of HO* to O* is nearly constant regardless of ΔG_{HO*}. However, we note that the slope of 2 for the linear scaling relation between ΔG_{O*} and ΔG_{HO*} has been shown to represent a limitation for catalyst design particularly for materials (metals and metal oxides) with surface metal centers serving as both adsorption and redox-active sites.[65,66] That scaling relation leads to a simultaneous enhancement of HO* formation and the following reaction from HO* to O* when reducing the ΔG_{HO*}, thus inevitably promoting both H_2O_2 and O_2 evolutions. By contrast, our subsurface approach separates the surface binding site from the redox center, breaking the scaling relation and modifying the activity trends observed for electrochemical water oxidation. Moreover, the data show that all of the redox-active metals investigated promote HO* formation by tuning the ΔG_{HO*} in a wide range of potentials, from 1.25 to 2.16 eV.

In the following discussion, we use the limiting potential (U_L) to evaluate the theoretical activity and selectivity for various electrochemical reaction pathways. The limiting potential (U_L) for a specific pathway is defined as the minimum potential necessary to allow all the electrochemical reaction steps by making them thermodynamically spontaneous. Thus, for the 2e-WOR toward H_2O_2, U_L is the highest potential between the following two electrochemical reaction steps: H_2O* to HO* and HO* to H_2O_2, while for the 4e-WOR leading to O_2 evolution, U_L is the highest potential when comparing the following four electrochemical steps: H_2O* to HO*, HO* to O*, O* to HOO*, and HOO* to O_2.

Figure 5b shows the minus limiting potential ($-U_L$) and the selectivity phase diagram for water oxidation toward different products. For H_2O_2 evolution, the U_L depends only on the ΔG_{HO*} with a minimum value of 1.77 V vs SHE (i.e., the standard redox potential of H_2O_2/H_2O).[9] While for O_2 evolution, the U_L is typically 2.58 V because of the linear relationship $\Delta G_{O*} = \Delta G_{HO*} + 2.58$ eV discussed above, until ΔG_{HO*} becomes larger than the ΔG of the second reaction step leading to the oxidation of HO* to O*. However, a ΔG_{HO*} larger than 2.40 eV would lead to HO* radical generation.[9] Therefore, the preferential H_2O_2 production has a wide window of ΔG_{HO*} values from 0.94 to 2.40 eV, with all our tested models distributed in this region. Moreover, the introduced redox-active metal ions can reduce the limiting potentials by moving the ΔG_{HO*} closer to 1.77 eV. The model with Co at B site is expected to exhibit excellent performance for electrochemical H_2O_2 production. It should be noted that the ΔG_{HO*} range for H_2O_2 generation on our models is substantially extended, compared to that on other metal oxides (ΔG_{HO*} ranges from 1.62 to 2.40 eV),[8] implying robust H_2O_2 evolution. Therefore, our results demonstrate that introducing subsurface redox-active metals not only boosts H_2O_2 evolution but also suppresses O_2 evolution by inheriting the unfavorable energetics of the oxidation of HO* to O* on the surface Ti^{4+} centers.

In the heterogeneous catalytic reaction on metal oxides, the surface metal centers often serve as both adsorption sites and redox-active centers. On TiO_2, however, the Ti^{4+} centers are already in their highest oxidation state so that they can only serve as adsorption sites for substrate water molecules. Therefore, it is unsurprising that TiO_2 is a poor electrocatalyst for water oxidation. It is known that doping with transition metal atoms can significantly lower the overpotentials for O_2 evolution.[67,68] However, both 2e-WOR and 4e-WOR are promoted when the doping ions are on the surface, due to the undesirable scaling relationship between ΔG_{O*} and ΔG_{HO*}, leading to poor selectivity for the 2e-WOR.[65,66]

Our subsurface strategy maintains the surface Ti^{4+} centers serving as adsorption sites while introducing an allosteric redox-active subsurface center that functions as an electron reservoir during the critical first step of the reaction. Therefore, the dual roles of substrate adsorption and redox-active center of surface-alloyed metal-oxide materials are separated in the subsurface design. By separating these two roles, we break the linear correlation between the ΔG values corresponding to $H_2O* \rightarrow HO*$ (ΔG_{HO*}) and the $HO* \rightarrow O*$ ($\Delta G_{O*} - \Delta G_{HO*}$) reactions. The former oxidation is affected by the subsurface redox-active metal ions, while the latter depends on the intrinsic properties; hence, the host metal oxide surface remains almost constant at 2.58 eV.

The concept of a subsurface doping element has been previously explored for bimetallic alloys to improve the catalytic activity of CO oxidation,[69,70] oxygen reduction reaction,[71−73] as well as the selectivity of dehydrogenation reactions.[74,75] However, to the best of our knowledge, our study represents the first analysis of subsurface redox-active metal centers embedded in a redox-inert metal oxide materials, as applied to improve the selectivity of the 2e-WOR toward H_2O_2 under lower overpotential. We envision that the same strategy could be used for the development of more selective electrocatalysts in other reactions, including CO_2 reduction, as already explored for Cu oxide,[76] and subsurface atoms on Cu surfaces to achieve high selectivity toward C_2 hydrocarbon products.[77]

4. CONCLUSIONS

We have shown both theoretically and experimentally that introducing subsurface redox-active transition metals into TiO_2 could effectively enhance the activity, selectivity, and robustness of the catalytic surface for electrochemical H_2O_2 production. The introduced redox-active metal centers serve as electron reservoirs and facilitate the formation of HO* by reducing the free energy change ΔG_{HO*} associated with the first step of the oxidation reaction. We find that the subsurface approach can dramatically reduce the limiting potential for H_2O_2 evolution by tuning ΔG_{HO*} toward the ideal value while preventing side reactions associated with the highly reactive HO* radical intermediate. Moreover, the introduced metals promote the H_2O_2 generation while preserving the large oxidation potential for O_2 evolution as on pristine TiO_2 surfaces, thus leading to predominant H_2O_2 production. This strategy is experimentally validated by electrolysis studies utilizing ALD grown electrodes, which demonstrates that the Mn-alloyed TiO_2 effectively reduces the WOR onset potential from 2.3 to 1.8 V vs RHE compared to pristine TiO_2 and achieves H_2O_2 selectivity as high as 90%. By introducing subsurface redox-active metals to a redox-inert metal oxide (TiO_2), we separate the roles of the adsorption and redox-active sites, breaking the linear relation between ΔG_{HO*} and $\Delta G_{O*} - \Delta G_{HO*}$ that limits the catalytic performance of many metals and metal oxides. In summary, the reported findings show that inert metal oxides with subsurface redox-active metal centers represent an attractive class of catalytic materials, offering a versatile strategy to breaking scaling relation in applications to multielectron electrocatalytic reactions.

■ ASSOCIATED CONTENT

Supporting Information

The Supporting Information is available free of charge at https://pubs.acs.org/doi/10.1021/acsaem.3c01057.

> Surface model stability test, detailed information DOS, spin density distributions, reaction energy diagrams, and H_2O_2 quantification methods (PDF)

■ AUTHOR INFORMATION

Corresponding Authors

Shu Hu − *Department of Chemical and Environmental Engineering and Energy Sciences Institute, Yale University, New Haven, Connecticut 06520-8286, United States;* orcid.org/0000-0002-5041-0169; Email: shu.hu@yale.edu

Victor S. Batista − *Department of Chemistry and Energy Sciences Institute, Yale University, West Haven, Connecticut 06516, United States;* orcid.org/0000-0002-3262-1237; Email: victor.batista@yale.edu

Ke R. Yang − *Department of Chemistry and Energy Sciences Institute, Yale University, West Haven, Connecticut 06516, United States;* orcid.org/0000-0003-0028-2717; Email: ke.yang@yale.edu

Authors

Dongyu Liu − *International Research Center for Renewable Energy (IRCRE), State Key Laboratory of Multiphase Flow in Power Engineering (MFPE), Xi'an Jiaotong University, Xi'an, Shaanxi 710049, China; Department of Chemistry and Energy Sciences Institute, Yale University, West Haven, Connecticut 06516, United States;* orcid.org/0000-0001-6941-1885

Devan Solanki − *Department of Chemical and Environmental Engineering and Energy Sciences Institute, Yale University, New Haven, Connecticut 06520-8286, United States;* orcid.org/0000-0003-1430-8295

Eli Stavitski − *National Synchrotron Light Source II, Brookhaven National Laboratory, Upton, New York 11973, United States*

Mingtao Li − *International Research Center for Renewable Energy (IRCRE), State Key Laboratory of Multiphase Flow in Power Engineering (MFPE), Xi'an Jiaotong University, Xi'an, Shaanxi 710049, China;* orcid.org/0000-0002-7171-5252

Complete contact information is available at: https://pubs.acs.org/10.1021/acsaem.3c01057

Author Contributions

D.L. and D.S. contributed equally. The manuscript was written through contributions of all authors. All authors have given approval to the final version of the manuscript.

Notes

The authors declare no competing financial interest.

■ ACKNOWLEDGMENTS

V.S.B. acknowledges the funding from DOE and computer time from the National Energy Research Scientific Computing Center (NERSC) and Yale Center for Research Computing (YCRC). S.H. acknowledges the funding from Yale Energy Science Institute and the Thistledown Foundation. S.H. and D.S. gratefully acknowledge the financial support of the National Science Foundation award no. CBET-2055416. D.L. acknowledges the support of the China Scholarship Council (CSC).

■ REFERENCES

(1) Shi, X.; Zhang, Y.; Siahrostami, S.; Zheng, X. Light-Driven $BiVO_4$−C Fuel Cell with Simultaneous Production of H_2O_2. *Adv. Energy Mater.* **2018**, *8*, 1801158.

(2) Hu, S. Membrane-less photoelectrochemical devices for H_2O_2 production: efficiency limit and operational constraint. *Sustainable Energy Fuels* **2019**, *3*, 101−114.

(3) Liu, J.; Zou, Y.; Jin, B.; Zhang, K.; Park, J. H. Hydrogen Peroxide Production from Solar Water Oxidation. *ACS Energy Lett.* **2019**, *4*, 3018−3027.

(4) Tang, J.; Zhao, T.; Solanki, D.; Miao, X.; Zhou, W.; Hu, S. Selective hydrogen peroxide conversion tailored by surface, interface, and device engineering. *Joule* **2021**, *5*, 1432−1461.

(5) Zhang, K.; Liu, J.; Wang, L.; Jin, B.; Yang, X.; Zhang, S.; Park, J. H. Near-complete suppression of oxygen evolution for photoelectrochemical H_2O oxidative H_2O_2 synthesis. *J. Am. Chem. Soc.* **2020**, *142*, 8641−8648.

(6) Hirakawa, H.; Shiota, S.; Shiraishi, Y.; Sakamoto, H.; Ichikawa, S.; Hirai, T. Au Nanoparticles Supported on $BiVO_4$: Effective Inorganic Photocatalysts for H_2O_2 Production from Water and O_2 under Visible Light. *ACS Catal.* **2016**, *6*, 4976−4982.

(7) Viswanathan, V.; Hansen, H. A.; Nørskov, J. K. Selective Electrochemical Generation of Hydrogen Peroxide from Water Oxidation. *J. Phys. Chem. Lett.* **2015**, *6*, 4224−4228.

(8) Roger, I.; Shipman, M. A.; Symes, M. D. Earth-abundant catalysts for electrochemical and photoelectrochemical water splitting. *Nat. Rev. Chem.* **2017**, *1*, 0003.

(9) Siahrostami, S.; Li, G.-L.; Viswanathan, V.; Nørskov, J. K. One- or two-electron water oxidation, hydroxyl radical, or H_2O_2 evolution. *J. Phys. Chem. Lett.* **2017**, *8*, 1157−1160.

(10) Campos-Martin, J. M.; Blanco-Brieva, G.; Fierro, J. L. G. Hydrogen peroxide synthesis: an outlook beyond the anthraquinone process. *Angew. Chem., Int. Ed.* **2006**, *45*, 6962−6984.

(11) Fukuzumi, S.; Yamada, Y.; Karlin, K. D. Hydrogen Peroxide as a Sustainable Energy Carrier: Electrocatalytic Production of Hydrogen Peroxide and the Fuel Cell. *Electrochim. Acta* **2012**, *82*, 493−511.

(12) Ciriminna, R.; Albanese, L.; Meneguzzo, F.; Pagliaro, M. Hydrogen Peroxide: A Key Chemical for Today's Sustainable Development. *ChemSusChem* **2016**, *9*, 3374−3381.

(13) Yang, S.; Verdaguer-Casadevall, A.; Arnarson, L.; Silvioli, L.; Čolić, V.; Frydendal, R.; Rossmeisl, J.; Chorkendorff, I.; Stephens, I. E. L. Toward the Decentralized Electrochemical Production of H_2O_2: A Focus on the Catalysis. *ACS Catal.* **2018**, *8*, 4064−4081.

(14) Jiang, Y.; Ni, P.; Chen, C.; Lu, Y.; Yang, P.; Kong, B.; Fisher, A.; Wang, X. Selective Electrochemical H_2O_2 Production through Two-Electron Oxygen Electrochemistry. *Adv. Energy Mater.* **2018**, *8*, 1801909.

(15) Perry, S. C.; Pangotra, D.; Vieira, L.; Csepei, L.-I.; Sieber, V.; Wang, L.; Ponce de León, C.; Walsh, F. C. Electrochemical synthesis of hydrogen peroxide from water and oxygen. *Nat. Rev. Chem.* **2019**, *3*, 442−458.

(16) Zhang, J.; Zhang, H.; Cheng, M.-J.; Lu, Q. Tailoring the Electrochemical Production of H_2O_2: Strategies for the Rational Design of High-Performance Electrocatalysts. *Small* **2020**, *16*, 1902845.

(17) Xia, C.; Xia, Y.; Zhu, P.; Fan, L.; Wang, H. Direct Electrosynthesis of Pure Aqueous H_2O_2 Solutions up to 20% by Weight Using a Solid Electrolyte. *Science* **2019**, *366*, 226−231.

(18) Jung, E.; Shin, H.; Lee, B.-H.; Efremov, V.; Lee, S.; Lee, H. S.; Kim, J.; Hooch Antink, W.; Park, S.; Lee, K.-S.; Cho, S.-P.; Yoo, J. S.; Sung, Y.-E.; Hyeon, T. Atomic-level tuning of Co−N−C catalyst for high-performance electrochemical H_2O_2 production. *Nat. Mater.* **2020**, *19*, 436−442.

(19) Sayama, K. Production of High-Value-Added Chemicals on Oxide Semiconductor Photoanodes under Visible Light for Solar Chemical-Conversion Processes. *ACS Energy Lett.* **2018**, *3*, 1093−1101.

(20) Hu, X.; Sun, Z.; Mei, G.; Zhao, X.; Xia, B. Y.; You, B. Engineering Nonprecious Metal Oxides Electrocatalysts for Two-Electron Water Oxidation to H_2O_2. *Adv. Energy Mater.* **2022**, *12*, 2201466.

(21) Kelly, S. R.; Shi, X.; Back, S.; Vallez, L.; Park, S. Y.; Siahrostami, S.; Zheng, X.; Nørskov, J. K. ZnO as an active and selective catalyst

for electrochemical water oxidation to hydrogen peroxide. *ACS Catal.* **2019**, *9*, 4593−4599.

(22) Park, S. Y.; Abroshan, H.; Shi, X.; Jung, H. S.; Siahrostami, S.; Zheng, X. $CaSnO_3$: an electrocatalyst for two-electron water oxidation reaction to form H_2O_2. *ACS Energy Lett.* **2019**, *4*, 352−357.

(23) Hu, X.; Mei, G.; Chen, X.; Liu, J.; Xia, B. Y.; You, B. Simultaneous Generation of H_2O_2 and Formate by Co-Electrolysis of Water and CO_2 over Bifunctional Zn/SnO_2 Nanodots. *Angew. Chem., Int. Ed.* **2023**, *135*, No. e202304050.

(24) Wan, S.; Dong, C.; Jin, J.; Li, J.; Zhong, Q.; Zhang, K.; Park, J. H. Tuning the Surface Wettability of a $BiVO_4$ Photoanode for Kinetically Modulating Water Oxidative H_2O_2 Accumulation. *ACS Energy Lett.* **2022**, *7*, 3024−3031.

(25) Li, J.; Solanki, D.; Zhu, Q.; Shen, X.; Callander, G.; Kim, J.; Li, Y.; Wang, H.; Hu, S. Microstructural origin of selective water oxidation to hydrogen peroxide at low overpotentials: a study on Mn-alloyed TiO_2. *J. Mater. Chem. A* **2021**, *9*, 18498−18505.

(26) Dong, K.; Liang, J.; Wang, Y.; Ren, Y.; Xu, Z.; Zhou, H.; Li, L.; Liu, Q.; Luo, Y.; Li, T.; Asiri, A. M.; Li, Q.; Ma, D.; Sun, X. Plasma-induced defective TiO_{2-x} with oxygen vacancies: A high-active and robust bifunctional catalyst toward H_2O_2 electrosynthesis. *Chem. Catal.* **2021**, *1*, 1437−1448.

(27) Baek, J. H.; Gill, T. M.; Abroshan, H.; Park, S.; Shi, X.; Nørskov, J.; Jung, H. S.; Siahrostami, S.; Zheng, X. Selective and efficient Gd-doped $BiVO_4$ photoanode for two-electron water oxidation to H_2O_2. *ACS Energy Lett.* **2019**, *4*, 720−728.

(28) Kresse, G.; Hafner, J. Ab initio molecular dynamics for liquid metals. *Phys. Rev. B: Condens. Matter Mater. Phys.* **1993**, *47*, 558−561.

(29) Kresse, G.; Hafner, J. Ab Initio Molecular-Dynamics Simulation of the Liquid-Metal−Amorphouss-Semiconductor Transition in Germanium. *Phys. Rev. B: Condens. Matter Mater. Phys.* **1994**, *49*, 14251−14269.

(30) Kresse, G.; Furthmüller, J. Efficiency of Ab-Initio Total Energy Calculations for Metals and Semiconductors Using a Plane-Wave Basis Set. *Comput. Mater. Sci.* **1996**, *6*, 15−50.

(31) Kresse, G.; Furthmüller, J. Efficient iterative schemes for ab initio total-energy calculations using a plane-wave basis set. *Phys. Rev. B: Condens. Matter Mater. Phys.* **1996**, *54*, 11169−11186.

(32) Blöchl, P. E. Projector augmented-wave method. *Phys. Rev. B: Condens. Matter Mater. Phys.* **1994**, *50*, 17953−17979.

(33) Kresse, G.; Joubert, D. From Ultrasoft Pseudopotentials to the Projector Augmented-Wave Method. *Phys. Rev. B: Condens. Matter Mater. Phys.* **1999**, *59*, 1758−1775.

(34) Perdew, J. P.; Burke, K.; Ernzerhof, M. Generalized Gradient Approximation Made Simple. *Phys. Rev. Lett.* **1996**, *77*, 3865−3868.

(35) Dudarev, S. L.; Botton, G. A.; Savrasov, S. Y.; Humphreys, C. J.; Sutton, A. P. Electron-energy-loss spectra and the structural stability of nickel oxide: an LSDA+U study. *Phys. Rev. B: Condens. Matter Mater. Phys.* **1998**, *57*, 1505−1509.

(36) Chen, T.; Sai Gautam, G.; Huang, W.; Ceder, G. First-principles study of the voltage profile and mobility of Mg intercalation in a chromium oxide spinel. *Chem. Mater.* **2018**, *30*, 153−162.

(37) Yu, J.; Yan, Q.; Chen, W.; Jain, A.; Neaton, J. B.; Persson, K. A. First-principles study of electronic structure and photocatalytic properties of $MnNiO_3$ as an alkaline oxygen-evolution photocatalyst. *Chem. Commun.* **2015**, *51*, 2867−2870.

(38) Mesa, C. A.; Francàs, L.; Yang, K. R.; Garrido-Barros, P.; Pastor, E.; Ma, Y.; Kafizas, A.; Rosser, T. E.; Mayer, M. T.; Reisner, E.; Grätzel, M.; Batista, V. S.; Durrant, J. R. Multihole water oxidation catalysis on haematite photoanodes revealed by operando spectroelectrochemistry and DFT. *Nat. Chem.* **2020**, *12*, 82−89.

(39) Yan, G.; Sautet, P. Surface structure of Co_3O_4 (111) under reactive gas-phase environments. *ACS Catal.* **2019**, *9*, 6380−6392.

(40) Grimme, S.; Antony, J.; Ehrlich, S.; Krieg, H. A consistent and accurate ab initio parametrization of density functional dispersion correction (DFT-D) for the 94 elements H-Pu. *J. Chem. Phys.* **2010**, *132*, 154104.

(41) Grimme, S.; Ehrlich, S.; Goerigk, L. Effect of the damping function in dispersion corrected density functional theory. *J. Comput. Chem.* **2011**, *32*, 1456−1465.

(42) Monkhorst, H. J.; Pack, J. D. Special points for Brillouin-zone integrations. *Phys. Rev. B: Solid State* **1976**, *13*, 5188−5192.

(43) Burdett, J. K.; Hughbanks, T.; Miller, G. J.; Richardson, J. W.; Smith, J. V. Structural-electronic relationships in inorganic solids: powder neutron diffraction studies of the rutile and anatase polymorphs of titanium dioxide at 15 and 295 K. *J. Am. Chem. Soc.* **1987**, *109*, 3639−3646.

(44) Diebold, U. The Surface Science of Titanium Dioxide. *Surf. Sci. Rep.* **2003**, *48*, 53−229.

(45) Lee, J.; Sorescu, D. C.; Deng, X.; Jordan, K. D. Water chain formation on TiO_2(110). *J. Phys. Chem. Lett.* **2013**, *4*, 53−57.

(46) Wang, Z.-T.; Wang, Y.-G.; Mu, R.; Yoon, Y.; Dahal, A.; Schenter, G. K.; Glezakou, V.-A.; Rousseau, R.; Lyubinetsky, I.; Dohnálek, Z. Probing equilibrium of molecular and deprotonated water on TiO_2(110). *Proc. Natl. Acad. Sci. U.S.A.* **2017**, *114*, 1801−1805.

(47) Helali, Z.; Markovits, A.; Minot, C.; Dhouib, A.; Abderrabba, M. Improved convergence of rutile-TiO_2(110) slab properties with thickness by one-side saturation. *Chem. Phys. Lett.* **2012**, *531*, 90−93.

(48) Heyd, J.; Scuseria, G. E.; Ernzerhof, M. Hybrid functionals based on a screened Coulomb potential. *J. Chem. Phys.* **2003**, *118*, 8207−8215.

(49) Van de Walle, C. G.; Neugebauer, J. Universal alignment of hydrogen levels in semiconductors, insulators and solutions. *Nature* **2003**, *423*, 626−628.

(50) Wang, V.; Xu, N.; Liu, J.-C.; Tang, G.; Geng, W.-T. VASPKIT: A user-friendly interface facilitating high-throughput computing and analysis using VASP code. *Comput. Phys. Commun.* **2021**, *267*, 108033.

(51) Nørskov, J. K.; Rossmeisl, J.; Logadottir, A.; Lindqvist, L.; Kitchin, J. R.; Bligaard, T.; Jónsson, H. Origin of the overpotential for oxygen reduction at a fuel-cell cathode. *J. Phys. Chem. B* **2004**, *108*, 17886−17892.

(52) Shamsipur, M.; Taherpour, A.; Sharghi, H.; Lippolis, V.; Pashabadi, A. A Low-Overpotential Nature-Inspired Molecular Chromium Water Oxidation Catalyst. *Electrochim. Acta* **2018**, *265*, 316−325.

(53) Blakemore, J. D.; Crabtree, R. H.; Brudvig, G. W. Molecular catalysts for water oxidation. *Chem. Rev.* **2015**, *115*, 12974−13005.

(54) Kärkäs, M. D.; Åkermark, B. Water Oxidation Using Earth-Abundant Transition Metal Catalysts: Opportunities and Challenges. *Dalton Trans.* **2016**, *45*, 14421−14461.

(55) Hu, S.; Shaner, M. R.; Beardslee, J. A.; Lichterman, M.; Brunschwig, B. S.; Lewis, N. S. Amorphous TiO_2 coatings stabilize Si, GaAs, and GaP photoanodes for efficient water oxidation. *Science* **2014**, *344*, 1005−1009.

(56) Herklotz, F.; Lavrov, E. V.; Weber, J. Infrared absorption of the hydrogen donor in rutile TiO_2. *Phys. Rev. B: Condens. Matter Mater. Phys.* **2011**, *83*, 235202.

(57) Brant, A. T.; Yang, S.; Giles, N. C.; Halliburton, L. E. Hydrogen Donors and Ti^{3+} Ions in Reduced TiO_2 Crystals. *J. Appl. Phys.* **2011**, *110*, 053714.

(58) George, S. M. Atomic Layer Deposition: An Overview. *Chem. Rev.* **2010**, *110*, 111−131.

(59) Siddiqi, G.; Luo, Z.; Xie, Y.; Pan, Z.; Zhu, Q.; Röhr, J. A.; Cha, J. J.; Hu, S. Stable Water Oxidation in Acid Using Manganese-Modified TiO_2 Protective Coatings. *ACS Appl. Mater. Interfaces* **2018**, *10*, 18805−18815.

(60) Gill, T. M.; Zheng, X. Comparing Methods for Quantifying Electrochemically Accumulated H_2O_2. *Chem. Mater.* **2020**, *32*, 6285−6294.

(61) Cheng, J.; VandeVondele, J.; Sprik, M. Identifying Trapped Electronic Holes at the Aqueous TiO_2 Interface. *J. Phys. Chem. C* **2014**, *118*, 5437−5444.

(62) Li, Y.-F.; Selloni, A. Pathway of Photocatalytic Oxygen Evolution on Aqueous TiO_2 Anatase and Insights Into the Different Activities of Anatase and Rutile. *ACS Catal.* **2016**, *6*, 4769−4774.

(63) Nakamura, R.; Nakato, Y. Primary Intermediates of Oxygen Photoevolution Reaction on TiO_2 (Rutile) Particles, Revealed by In Situ FTIR Absorption and Photoluminescence Measurements. *J. Am. Chem. Soc.* **2004**, *126*, 1290−1298.

(64) Gill, T. M.; Vallez, L.; Zheng, X. Enhancing Electrochemical Water Oxidation toward H_2O_2 via Carbonaceous Electrolyte Engineering. *ACS Appl. Energy Mater.* **2021**, *4*, 12429−12435.

(65) Rossmeisl, J.; Logadottir, A.; Nørskov, J. K. Electrolysis of Water on (Oxidized) Metal Surfaces. *Chem. Phys.* **2005**, *319*, 178−184.

(66) Rossmeisl, J.; Qu, Z. W.; Zhu, H.; Kroes, G. J.; Nørskov, J. K. Electrolysis of Water on Oxide Surfaces. *J. Electroanal. Chem.* **2007**, *607*, 83−89.

(67) García-Mota, M.; Vojvodic, A.; Metiu, H.; Man, I. C.; Su, H.-Y.; Rossmeisl, J.; Nørskov, J. K. Tailoring the Activity for Oxygen Evolution Electrocatalysis on Rutile TiO_2(110) by Transition-Metal Substitution. *ChemCatChem* **2011**, *3*, 1607−1611.

(68) Liu, B.; Chen, H. M.; Liu, C.; Andrews, S. C.; Hahn, C.; Yang, P. Large-Scale Synthesis of Transition-Metal-Doped TiO_2 Nanowires with Controllable Overpotential. *J. Am. Chem. Soc.* **2013**, *135*, 9995−9998.

(69) Su, H.-Y.; Bao, X.-H.; Li, W.-X. Modulating the Reactivity of Ni-Containing Pt(111)-Skin Catalysts by Density Functional Theory Calculations. *J. Chem. Phys.* **2008**, *128*, 194707.

(70) Mu, R.; Fu, Q.; Xu, H.; Zhang, H.; Huang, Y.; Jiang, Z.; Zhang, S.; Tan, D.; Bao, X. Synergetic Effect of Surface and Subsurface Ni Species at Pt−Ni Bimetallic Catalysts for CO Oxidation. *J. Am. Chem. Soc.* **2011**, *133*, 1978−1986.

(71) Kitchin, J. R.; Nørskov, J. K.; Barteau, M. A.; Chen, J. G. Modification of the Surface Electronic and Chemical Properties of Pt(111) by Subsurface 3d Transition Metals. *J. Chem. Phys.* **2004**, *120*, 10240−10246.

(72) Stamenkovic, V.; Mun, B. S.; Mayrhofer, K. J. J.; Ross, P. N.; Markovic, N. M.; Rossmeisl, J.; Greeley, J.; Nørskov, J. K. Changing the Activity of Electrocatalysts for Oxygen Reduction by Tuning the Surface Electronic Structure. *Angew. Chem., Int. Ed.* **2006**, *45*, 2897−2901.

(73) Stephens, I. E. L.; Bondarenko, A. S.; Perez-Alonso, F. J.; Calle-Vallejo, F.; Bech, L.; Johansson, T. P.; Jepsen, A. K.; Frydendal, R.; Knudsen, B. P.; Rossmeisl, J.; Chorkendorff, I. Tuning the Activity of Pt(111) for Oxygen Electroreduction by Subsurface Alloying. *J. Am. Chem. Soc.* **2011**, *133*, 5485−5491.

(74) Cai, W.; Mu, R.; Zha, S.; Sun, G.; Chen, S.; Zhao, Z.-J.; Li, H.; Tian, H.; Tang, Y.; Tao, F.; Zeng, L.; Gong, J. Subsurface Catalysis-Mediated Selectivity of Dehydrogenation Reaction. *Sci. Adv.* **2018**, *4*, No. eaar5418.

(75) Wu, Z.; Bukowski, B. C.; Li, Z.; Milligan, C.; Zhou, L.; Ma, T.; Wu, Y.; Ren, Y.; Ribeiro, F. H.; Delgass, W. N.; Greeley, J.; Zhang, G.; Miller, J. T. Changes in Catalytic and Adsorptive Properties of 2 nm Pt_3Mn Nanoparticles by Subsurface Atoms. *J. Am. Chem. Soc.* **2018**, *140*, 14870−14877.

(76) Mandal, L.; Yang, K. R.; Motapothula, M. R.; Ren, D.; Lobaccaro, P.; Patra, A.; Sherburne, M.; Batista, V. S.; Yeo, B. S.; Ager, J. W.; Martin, J.; Venkatesan, T. Investigating the Role of Copper Oxide in Electrochemical CO_2 Reduction in Real Times. *ACS Appl. Mater. Interfaces* **2018**, *10*, 8574−8584.

(77) Zhou, Y.; Che, F.; Liu, M.; Zou, C.; Liang, Z.; De Luna, P.; Yuan, H.; Li, J.; Wang, Z.; Xie, H.; Li, H.; Chen, P.; Bladt, E.; Quintero-Bermudez, R.; Sham, T.-K.; Bals, S.; Hofkens, J.; Sinton, D.; Chen, G.; Sargent, E. H. Dopant-induced electron localization drives CO_2 reduction to C_2 hydrocarbons. *Nat. Chem.* **2018**, *10*, 974−980.